Applied Catalysis B: Environmental 182 (2016) 533–540

Contents lists available at ScienceDirect

Applied Catalysis B: Environmental

journal homepage: www.elsevier.com/locate/apcatb

Hydroxide $SrSn(OH)_6$: A new photocatalyst for degradation of benzene and rhodamine B

Yanpei Luo, Jing Chen, Jiawen Liu, Yu Shao, Xiaofang Li, Danzhen Li*

Research Institute of Photocatalysis, State Key Laboratory of Photocatalysis on Energy and Environment, Fuzhou University, Fuzhou 350002, PR China

ARTICLE INFO

Article history:
Received 31 August 2015
Received in revised form
19 September 2015
Accepted 26 September 2015

Keywords:
$SrSn(OH)_6$
Photocatalysis
Homogeneous precipitation
Decomposition of benzene

ABSTRACT

A novel photocatalyst $SrSn(OH)_6$ was successfully synthesized via a facile homogeneous precipitation method. The photocatalytic activities of the as-prepared $SrSn(OH)_6$ were evaluated by the degradation of benzene and rhodamine B under the irradiation of 254 nm UV light. The experimental results indicated that $SrSn(OH)_6$ synthesized at a lower pH value had a better photocatalytic activity. Furthermore, compared with commercial TiO_2 (P25), the as-prepared $SrSn(OH)_6$ showed a better photocatalytic performance for degradation of benzene under 254 nm UV irradiation. During 32 h of photocatalytic process, the conversion ratio of benzene over $SrSn(OH)_6$ and TiO_2 (P25) were 31% and 11%, and the mineralization ratio were about 55% and 16%, respectively. Based on the characterization results and the detection of active species, the high photocatalytic activity of $SrSn(OH)_6$ may attribute to the $^{\bullet}OH$ radicals, which play an important role in the degradation of both benzene and rhodamine B. This article enriches the study of hydroxide stannates and has reference significance for other hydroxide stannates. This work shows that the hexagonal phase of hydroxide stannate may not have much better or worse photocatalytic performance than cubic phase does. So, the crystal phase cannot be the main reason to influence the photocatalytic performance of hydroxide stannates. More research of other hydroxide stannates should focus on making good use of the hydroxyl groups in its structure.

1. Introduction

As an important solvent and raw material, benzene is widely used in manufacturing processes and petroleum-based industries [1]. Due to its volatile, high carcinogenicity and environmental persistence, benzene has been regarded as a prior hazardous substance that requires highly efficient treatment technologies [2,3]. Consequently, the development of an efficient technology for the degradation of benzene remains an imperative topic at ambient condition.

Rational use of photocatalytic technology is proved to be the most promising technique for persistent organic pollutant removal [4,5]. Owing to its excellent photocatalytic performance, high chemical stability, low cost and environmental friendliness, titanium dioxide has been one of the most widely used photocatalysts [6,7]. However, in dealing with the gas aromatic pollutants, the accumulation of less-reactive by-products on the surface of photocatalyst always leads to the deactivation of catalyst [8,9]. At the same time, titanium dioxide also has the disadvantages of low quantum efficiency and underutilization of solar energy. Based on the above two points, to explore new photocatalyst for treating gas aromatic pollutants like benzene is still necessary.

Much progress has been made in photocatalytic decomposition of benzene. Some photocatalysts (such as $In(OH)_3$ [10], InOOH [11], $CaSn(OH)_6$ [12], $ZnSn(OH)_6$ [13], $CdSnO_3{\cdot}3H_2O$ [14] etc.) have been proved to have high photocatalytic activities. Among these catalysts, a hydroxyl structure is indispensable to the degradation of benzene, which can be explained by the abundance of surface OH groups accepted photogenerated holes to yield highly reactive OH radicals [13]. Besides, it has been reported that their high activities could be attributed to the central metal ions (In^{3+}, Sn^{4+}) with d^{10} electronic configuration, which were favorable for the separation of photogenerated electron/hole pairs [15]. Compared with the rarity and high cost of In, the low cost Sn based hydroxides are more realistic for practical application. Therefore, it stimulates our interest to further investigate other hydroxide stannates. $SrSn(OH)_6$ with different morphologies has been used as precursor materials for making $SrSnO_3$, which is used as anode materials for Li-ion battery [16]. To the best of our knowledge, few reports have been found about $SrSn(OH)_6$ on the application of benzene degradation. In addition, the structure of $CaSn(OH)_6$, $ZnSn(OH)_6$ and $CdSnO_3{\cdot}3H_2O$ is cubic and the structure of $SrSn(OH)_6$ is hexagonal, which makes

* Corresponding author. Fax: +86 591 83779256.
E-mail address: dzli@fzu.edu.cn (D. Li).

http://dx.doi.org/10.1016/j.apcatb.2015.09.051
0926-3373/

us more interested in whether $SrSn(OH)_6$ has the similar high photocatalytic activity or not. Herein, we have successfully synthesized $SrSn(OH)_6$ by a homogeneous precipitation method and the as-prepared sample shows nearly three times higher activity and durability than that of commercial TiO_2 (P25) under the same conditions. The photocatalytic degradation of rhodamine B (RhB) has also been investigated. Furthermore, a possible mechanism of the new photocatalyst with high photocatalytic activity is proposed.

2. Experimental

2.1. Preparation of $SrSn(OH)_6$

All of the reagents were analytical-grade and used without further purification. First, 25 mL of 1.2 mol L^{-1} NaOH aqueous solution was mixed with 25 mL of 0.2 mol L^{-1} $SnCl_4$ aqueous solution under magnetic stirring, and then a clear aqueous solution was obtained. Second, the obtained solution was added drop wise into 50 mL of 0.1 mol L^{-1} $SrCl_2$ aqueous solution. Third, the above mixed aqueous solution was stirred for 30 min to obtain the white slurry. During that time, hydrochloric acid (0.1 mol L^{-1}) was added to adjust different pH value. Then, the slurry was washed repeatedly with distilled water to remove excess salts. The product was finally dried at 80 °C in air. The corresponding products denoted as pH *X.X* stands for the pH value.

2.2. Characterization of samples

The phase constituents of the products were measured by X-ray powder diffractometer (XRD, Bruker D8 Advance with Ni-filtered Cu Kα radiation) in the 2θ range from 10° to 70°. The accelerating voltage and the applied current were 40 KV and 40 mA, respectively. The morphologies of the obtained products were observed by field-emission scanning electron microscopy (FE-SEM, FEI Nova NANOSEM 230, operated at an accelerating voltage of 15 kV) and transmission electron microscopy (TEM, FEI Tecnai G2 F20 S-TWIN, operated at an accelerating voltage of 200 kV). The diffuse reflection spectra (DRS) of the samples were collected by Cary 500 UV–vis-NIR spectrometers with $BaSO_4$ as the background from 200 nm to 500 nm. The Brunauer–Emmett–Teller (BET) specific surface area of the composites were analyzed by nitrogen adsorption at 77 K on an Autosorb-1C-TCD physical adsorption instrument (American Quantach—Rome) using a Micrometrics ASAP 2020 system. X-ray photoelectron spectroscopy (XPS) analysis were conducted on an ESCALAB 250 photoelectron spectroscopy (Thermo Fisher Scientific) at 3.0×10^{-10} mbar using Al Kα radiation (E = 1486.6 eV). Electron spin resonance (ESR) signal-trapped by 5,5-dimethyl-*l*-pyrroline-*n*-oxide (DMPO) were collected with an EPR spectrometer (ESP 300E, Bruker). A spot UV-light source of Hamamatsu Co. (LC8), equipped with a 254 nm filter, was used as a photo-excitation light source. The photo-electrochemical data was collected by a CHI-660D electrochemical workstation (Chenhua Instruments, Co., Shanghai). The photo-electrochemical experiment was carried out in a conventional three-electrode cell with a quartz window. The sample was deposited on a sheet of fluorine-tin-oxide (FTO) glass to serve as the working electrode with 0.5 cm × 0.5 cm area. A platinum wire and an Ag/AgCl electron were used as the counter and reference electrodes, respectively. The electrolyte was 0.1 mol L^{-1} Na_2SO_4 solution.

2.3. The test of photocatalytic performance

The photocatalytic oxidation experiments were operated in a tubular quartz micro-reactor with a continuous-flow mode. The quartz vessel was surrounded by three 4W fluorescent UV bulbs (TUV 4W/G4 T5, Philips, wavelength 254 nm). The vessel is 11 cm in length and 2.4 mm in diameter, in which only 0.4 g of catalyst (50–70 mesh) was loaded. Diluted benzene vapor was introduced into the reactor along with a continuous O_2 gas stream at a flow rate of 20 cm^3 min^{-1}. Prior to irradiation, the adsorption–desorption equilibrium of benzene on the photocatalyst was carried out. The equilibrium concentration of benzene was about 280 ± 20 ppm and CO_2 was zero. The concentrations of benzene and CO_2 were analyzed by an on-line gas chromatograph (HP6890), equipped with a thermal conductivity detector, a flame ionization detector, and a Porapak R column. The conversion ratio and mineralization ratio of benzene for the reaction are calculated according to the steady-state data by Eqs. (A.1) and (A.2), respectively. $[C_6H_6]_{initial}$ means the equilibrium concentration of benzene before the reaction, and $[C_6H_6]_{steady}$ means the essentially constant concentration of benzene during the reaction.

$$\text{conversion}\,(\%) = \frac{[C_6H_6]_{initial} - [C_6H_6]_{steady}}{[C_6H_6]_{initial}} \times 100\% \quad \text{(A.1)}$$

$$\text{mineralization}(\%) = \frac{[CO_2]_{steady}}{[C_6H_6]_{initial} - [C_6H_6]_{steady}} \times 100\% \quad \text{(A.2)}$$

The photocatalytic degradations of rhodamine B (RhB) in the liquid phase were also conducted using a quartz tube reactor system. The quartz vessel was surrounded by four 4 W fluorescent UV bulbs (TUV 4W/G4 T5, Philips, wavelength 254 nm). The vessel is 18 cm in length and 5 cm in diameter, in which 75 mg catalysts were loaded into 150 mL of 10 μmol L^{-1} RhB solution. Prior to irradiation, the suspensions were magnetically stirred in dark for 2 h to ensure the establishment of adsorption–desorption equilibrium. After irradiation, 3 mL of liquid was taken at a certain time interval and centrifuged to remove the catalyst. Then the supernatant was analyzed using a Varian UV–vis Spectrophotometer (Carry-50, Varian Co.). The photocatalytic conversion ratio was recognized as C/C_0. C and C_0 were the concentration of RhB at the momentary and initial time, respectively.

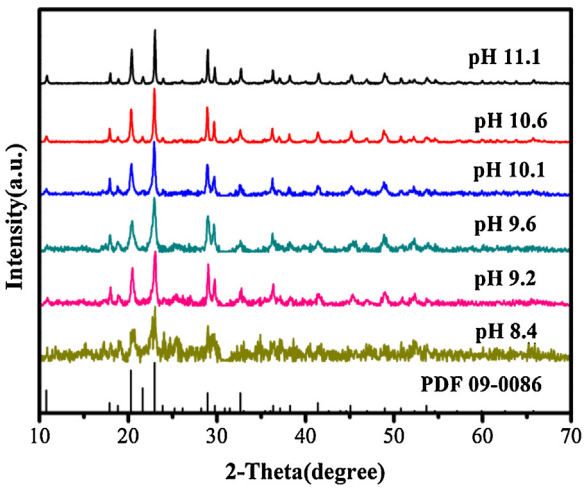

Fig. 1. XRD patterns of the $SrSn(OH)_6$ prepared at different solution pH.

3. Results and discussion

3.1. Characterization of $SrSn(OH)_6$

The XRD patterns of $SrSn(OH)_6$ samples synthesized at different pH value were shown in Fig. 1. All these diffraction peaks could be index to the $SrSn(OH)_6$ (JCPDS 09-0086), and there was no extra peaks in the pattern. Distinctive peaks at 10.74°, 20.31°, 21.60°, 22.96°, 28.97° and 32.66° were matched well with the diffraction peaks of the (1 1 0), (3 0 1), (0 0 3), (2 2 1), (0 0 4) and (5 0 1) crystal

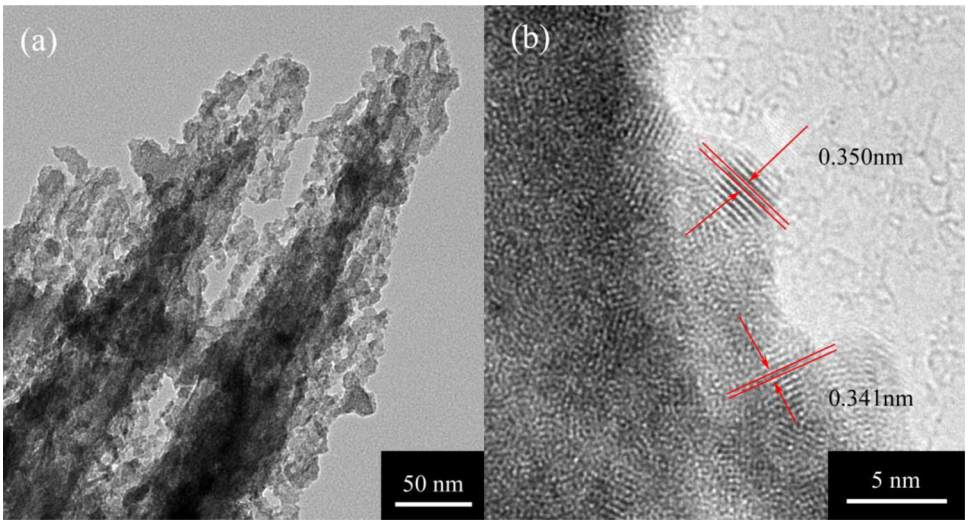

Fig. 2. Typical (a) TEM and (b) HRTEM images of $SrSn(OH)_6$ prepared at pH 9.2.

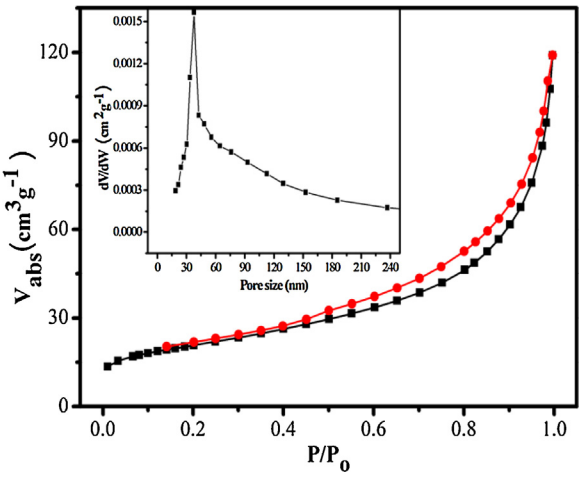

Fig. 3. Nitrogen adsorption–desorption isotherm and the pore size distribution plot for $SrSn(OH)_6$ prepared at pH 9.2 (desorption branch of isotherm).

planes of $SrSn(OH)_6$. Because of adding hydrochloric acid to adjust the pH value, the peaks became weak. That is the reason why we choose pHs 9.2, 9.6, 10.1, 10.6 and 11.1 for further investigation.

The morphology of a typical $SrSn(OH)_6$ prepared at pH 9.2 was investigated with TEM and the TEM images were shown in Fig. 2. A rod-like morphology consisted by nanoparticles could be observed over the as-prepared $SrSn(OH)_6$ in Fig. 2a. Furthermore, the HRTEM image in Fig. 2b revealed that the interplanar crystal spacing of 0.341 nm and 0.350 nm were corresponding to the (2 2 2) and (4 0 0) crystal plane of the as-prepared $SrSn(OH)_6$.

The specific surface area and pore diameter distribution of $SrSn(OH)_6$ prepared at different pH value were characterized by the BET analysis. Fig. 3 showed the N_2 adsorption–desorption isotherm for a typical $SrSn(OH)_6$ synthesized at pH 9.2. The stepwise adsorption and desorption observed over the isotherm of the as-prepared sample could be belong to the type-IV isotherm, which was indicative of a mesoporous solid. The pore size distribution plot demonstrated that the average pore size of the sample was 30.3–42.7 nm. Furthermore, the BET specific surface areas of the samples synthesized at different pH value were calculated in Table 1. With the decrease of pH value, the specific surface areas of the samples increase gradually. This is probably because the hydrochloric acid may corrode the surface of the samples and enlarge the specific surface area.

Table 1
The BET specific surface area and band gap of $SrSn(OH)_6$ prepared at different pH value (reaction temperature: 30 °C).

	pH 11.1	pH 10.6	pH 10.1	pH 9.6	pH 9.2
BET (m^2 g^{-1})	29.46	40.07	52.67	65.82	72.81
Band gap (eV)	3.70	3.74	3.76	3.81	3.86

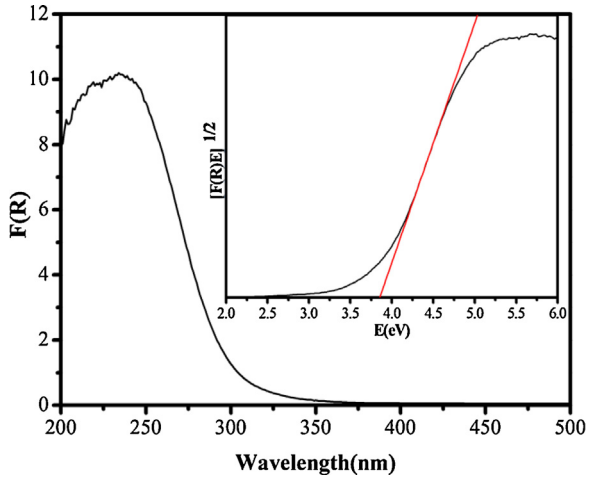

Fig. 4. The DRS and optical band gap energy (E_g) of $SrSn(OH)_6$ prepared at pH 9.2.

Optical absorption properties and band gap of $SrSn(OH)_6$ prepared at different pH value were measured with DRS. Fig. 4 shows the UV–vis diffuse reflectance spectra of a typical $SrSn(OH)_6$ synthesized at pH 9.2. An optical absorption started from 370 nm could be observed in the spectra. Moreover, it is well-known that the relation between absorption coefficient and band gap energy of an indirect gap semiconductor can be described by the formula $[F(R)E]^{1/2} = A(E - E_g)$. E and E_g are the photon energy and optical band gap energy, respectively [17]. Extrapolating the linear relation to $[F(R)E]^{1/2} = 0$ could get the band gap E_g of the samples. Therefore, as shown in the inset of Fig. 4, the band gap of $SrSn(OH)_6$ synthesized at pH 9.2 was calculated approximately to be 3.86 eV and the absorption edge was located at 321.2 nm. Table 1 shows the band gaps of the samples synthesized at different pH value.

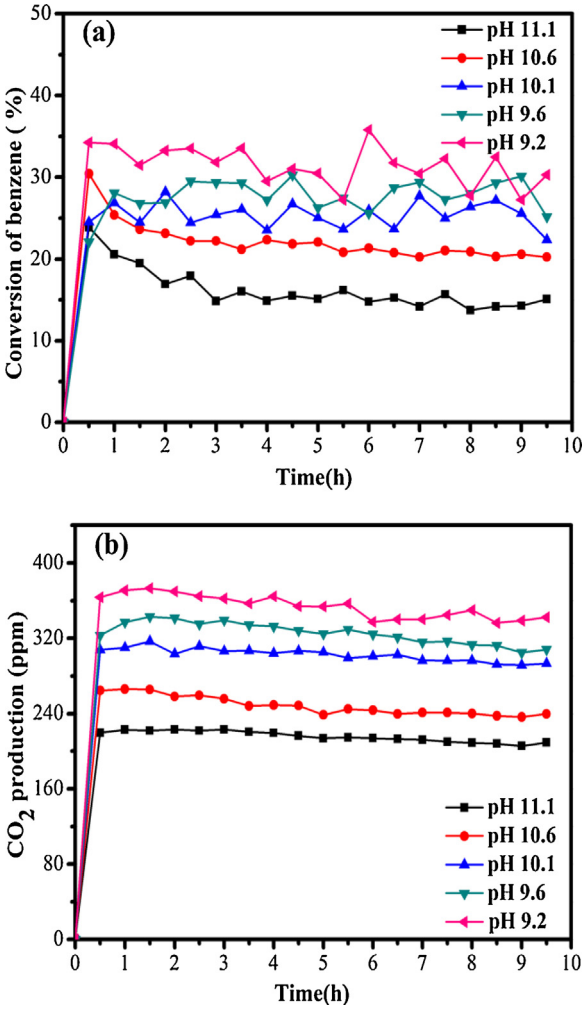

Fig. 5. (a) Conversion of C_6H_6 and (b) the amount of produced CO_2 over the $SrSn(OH)_6$ samples synthesized at different pH value.

The band gap of the samples also increase in the order of pHs 9.2 > 9.6 > 10.1 > 10.6 > 11.1, which means that $SrSn(OH)_6$ synthesized at pH 9.2 owns stronger oxidation potential.

3.2. Photocatalytic activity of $SrSn(OH)_6$

Gas-phase photocatalytic degradation of benzene was evaluated in a dry O_2 gas stream under UV irradiation at room temperature. Fig. 5 shows the photocatalytic activities of $SrSn(OH)_6$ synthesized at different pH values. The conversion ratios of benzene were 16%, 22%, 25%, 28% and 31% for the $SrSn(OH)_6$ prepared at pHs 11.1, 10.6, 10.1, 9.6 and 9.2, respectively. The concentration of produced CO_2 was 216 ppm, 248 ppm, 303 ppm, 325 ppm, and 354 ppm corresponding to pHs 11.1, 10.6, 10.1, 9.6 and 9.2, respectively. Thus, with the decrease of the pH value, the photocatalytic activities of the samples increase. The high photocatalytic activity of pH 9.2 can attribute to a larger surface area and a broader band gap. A larger surface area means more activity sites, which have more chance to react with absorbed benzene. At the same time, a broader band gap means a stronger oxidation potential, which enhances the redox ability of photogenerated holes and electrons. That is why the photocatalytic activity of pH 9.2 is the highest in all the samples. In addition, the tests of repeatability have been supplemented in Fig. S5, indicating that there is good repeatability for the gas-phase photocatalytic activity.

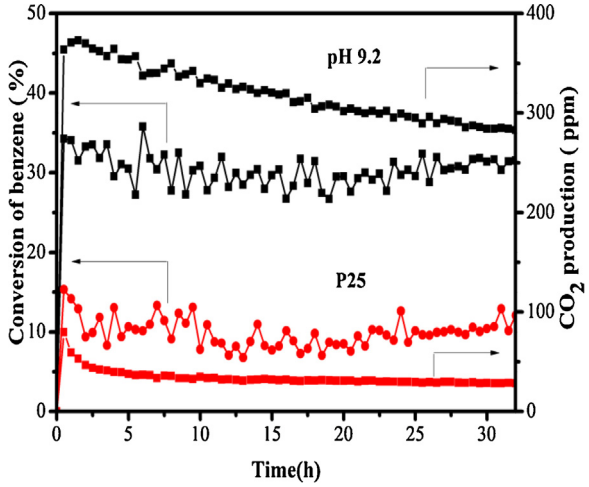

Fig. 6. Conversion of C_6H_6 and the amount of produced CO_2 over the $SrSn(OH)_6$ (pH 9.2) as a function of reaction time, with P25 as reference.

To better understand the performance of the catalysts, $SrSn(OH)_6$ prepared at pH 9.2 was selected to compare with commercial TiO_2 (P25). Fig. 6 shows the photocatalytic degradation of benzene over $SrSn(OH)_6$ and P25 under 254 nm UV light irradiation. For P25, the initial conversion ratio of benzene was about 12% and the amount of product CO_2 was 54 ppm corresponding to a mineralization ratio of 27%. After reacted for 32 h, the conversion of benzene maintained at about 11%. However, the CO_2 production reduced from 54 ppm to 28 ppm, and the mineralization ratio decreased from 27% to 16%. The new photocatalyst $SrSn(OH)_6$ presented a higher and more stable activity than P25 during the photocatalytic degradation of benzene under the same conditions. The conversion ratio of benzene maintained stably at 31%, which was as three times as that of P25. The amount of produced CO_2 was about 284 ppm, corresponding to the mineralization ratio of 55%. After 32 h of photocatalytic process, the conversion ratio almost unchanged, but the mineralization ratio became lower than the original, indicating that there is a little inactivation. The color of $SrSn(OH)_6$ changed from white to light pink, which suggested that few carbons were accumulated on the surface activity sites of the photocatalyst, which had no obvious influence on its activity (Fig. 6).

Liquid-phase photocatalytic degradation of RhB over $SrSn(OH)_6$ synthesized at pH 9.2 revealed that the photocatalytic conversion ratio (PCR) of RhB was 97% after UV irradiation for 30 min (Fig. 7). Therefore, the new catalyst $SrSn(OH)_6$ not only exhibited high efficiency photodecomposition of benzene in gas-phase, but also showed good performance for RhB degradation in liquid-phase. In addition, the tests of repeatability have been supplemented in Fig. S7, indicating that there is good repeatability for the liquid-phase photocatalytic activity.

As we know, the stability of a photocatalyst is important to its application. To investigate the stability of the new photocatalyst, further characterizations XRD and XPS of the original and used samples were performed. Fig. 8 showed the XRD patterns of $SrSn(OH)_6$ before and after reaction. The position and the intensities of peaks were nearly the same, which indicated that the photocatalyst was stable. XPS was used to test the surface chemical shift of the photocatalyst, so the detailed spectra for Sn 3d were shown in Fig. 9. The binding energies of Sn 3d before and after use were nearly the same. It illustrated that there were no change in the chemical state of Sn during photocatalytic process. The X-ray photoelectron survey spectra of $SrSn(OH)_6$ in Fig. 9 can also confirm the stability of the catalysts.

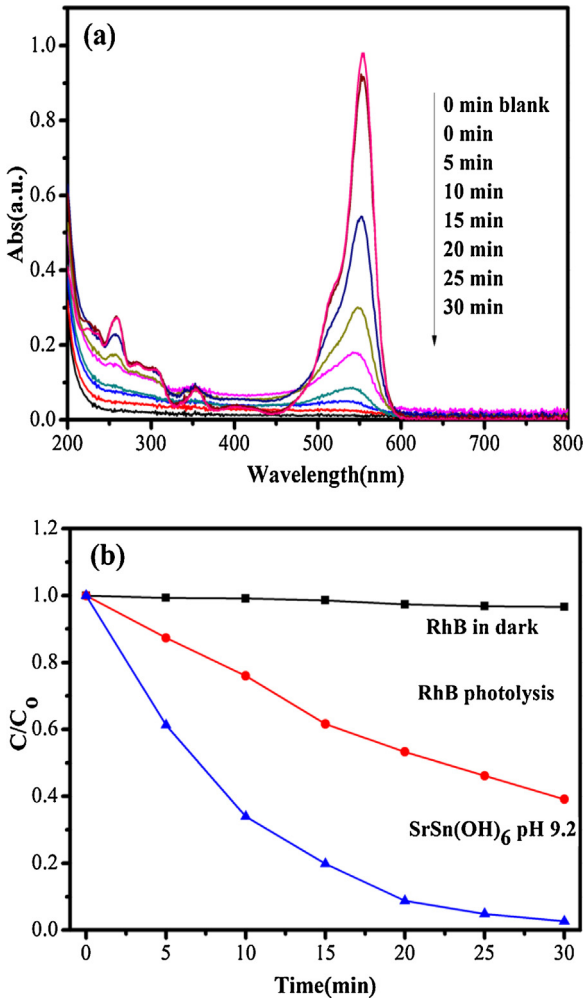

Fig. 7. (a) The temporal absorption spectral pattern of RhB in the presence of $SrSn(OH)_6$ (pH 9.2) under UV irradiation and (b) temporal changes of RhB concentration as monitored by UV–vis absorption spectra at 554 nm on $SrSn(OH)_6$.

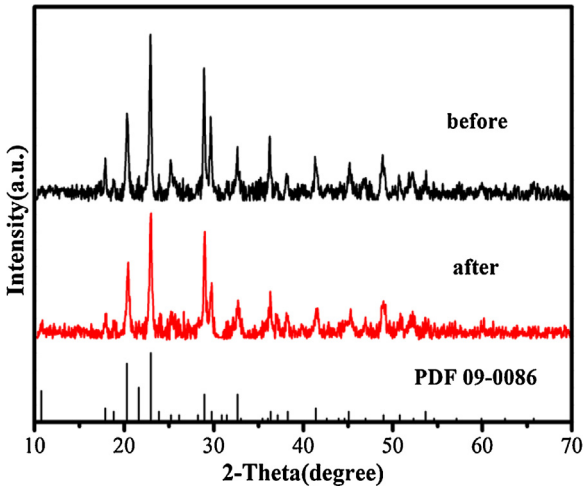

Fig. 8. XRD patterns of $SrSn(OH)_6$ (pH 9.2) before and after reaction.

3.3. Photocatalytic mechanism

In addition to the large surface area and the wide band gap, the separation and transporting rate of the photogenerated electrons and holes in the catalyst also play important role

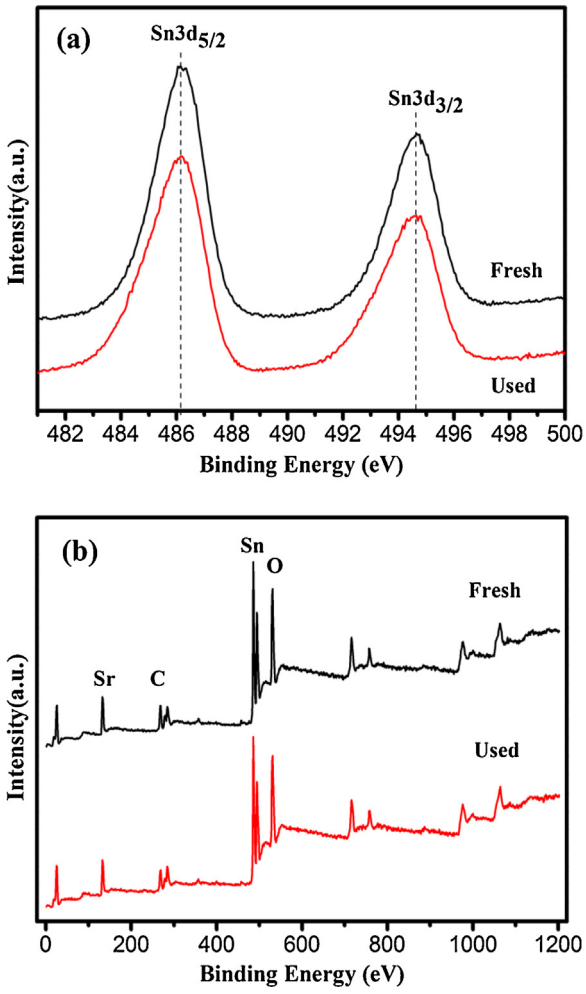

Fig. 9. (a) High-resolution XPS spectra and (b) survey spectra of $SrSn(OH)_6$ (pH 9.2) before and after reaction.

in the overall catalytic activity of photocatalyst. The transient photocurrent response has been demonstrated to be a useful technique for investigating the separation efficiency of photogenerated electron–hole pairs [18,19]. The anodic photocurrent produced by the UV-light irradiation was observed with good reproducibility. As shown in Fig. 10a, the photocurrent response of $SrSn(OH)_6$ synthesized at pH 9.2 was obviously better than that of other samples, which suggested that $SrSn(OH)_6$ synthesized at pH 9.2 possessed more efficient separation and longer lifetime of photogenerated electron–hole pairs than the others. In addition, electrochemical impedance spectroscopy (EIS) nyquist plots of $SrSn(OH)_6$ synthesized at different pH value was shown in Fig. 10b. The impedance arc radius of $SrSn(OH)_6$ synthesized at pH 9.2 was smaller than the others. The results of EIS Nyquist plots demonstrated that the efficiency of the separation of photogenerated electron–hole pairs increased with the pH value decreasing, which was in good agreement with the result of photocurrent measurements.

As we all know, two important radicals ($^{\bullet}OH$ and $^{\bullet}O_2^-$) would produce in the process of photocatalytic reaction. The generation of $^{\bullet}OH$ and $^{\bullet}O_2^-$ radicals was confirmed by the ESR spin trap with DMPO technique in this study. As shown in Fig. 11a, four characteristic peaks of DMPO-$^{\bullet}OH$ with intensity of 1:2:2:1 had been obviously observed in water suspension. As shown in Fig. 11b, six characteristic peaks of DMPO-$^{\bullet}O_2^-$ adduct had been also obviously observed in methanol dispersions. The intensity of DMPO-$^{\bullet}OH$ and

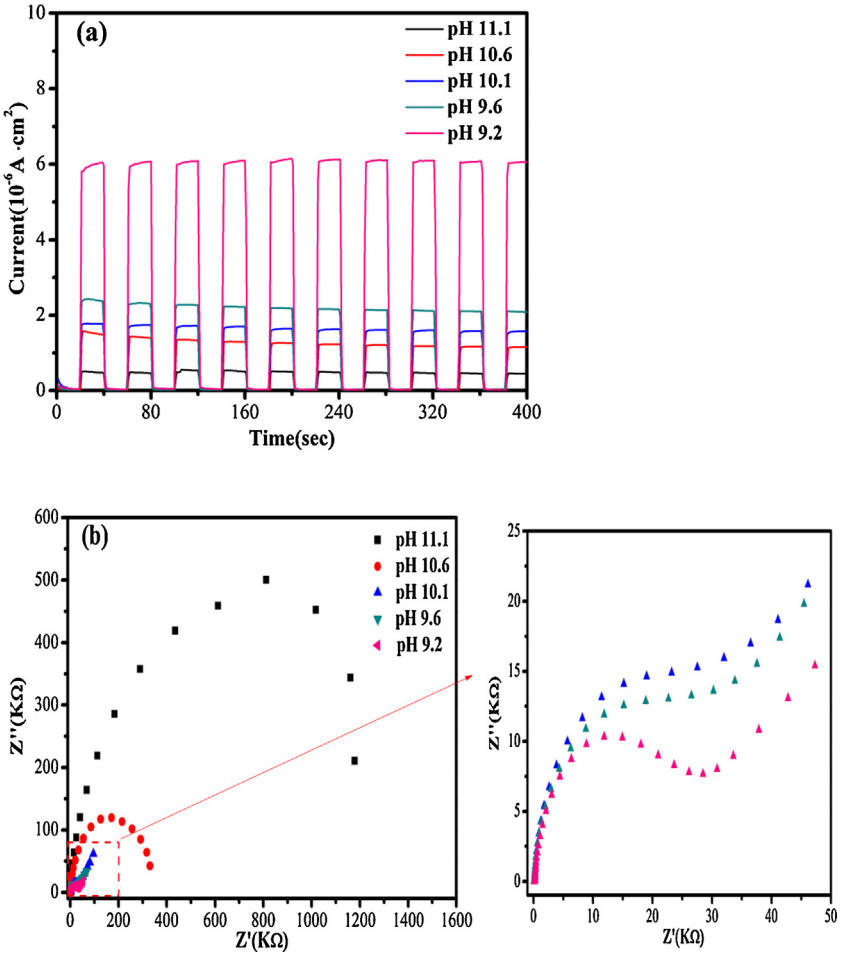

Fig. 10. (a) Transient photocurrent responses and (b) EIS Nyquist plots without any bias potential of $SrSn(OH)_6$ synthesized at different pH value under a UV-light source.

DMPO-$^{\bullet}O_2^-$ increased with the pH value decreasing, which was consist with the photocatalytic activity of $SrSn(OH)_6$ samples in the degradation of benzene. Furthermore, compared with P25, pHs 10.6 and 11.1 showed a weaker intensity of DMPO-$^{\bullet}O_2^-$, but had a better photocatalytic activity. It can be inferred that the $^{\bullet}O_2^-$ radicals is not the most important active species but $^{\bullet}$OH is. Because the intensity of DMPO-$^{\bullet}$OH over $SrSn(OH)_6$ is much higher than that of P25. Focusing on the electron–hole transfer process and the generation of the hydroxyl groups on the new photocatalyst, the following reaction mechanism was proposed. When $SrSn(OH)_6$ was excited to produce electron/hole pairs under 254 nm UV light irradiation (Eq. (B.1)), the abundance of —OH on the new photocatalyst could accept photo-generated holes to yield highly reactive $^{\bullet}$OH radicals and the separated electrons were transferred and reacted with absorbed O_2 and formed $^{\bullet}O_2^-$ (Eqs. (B.2) and (B.3)). During the same irradiation time, the higher production of $^{\bullet}$OH and $^{\bullet}O_2^-$ mean the higher separation and transporting rate of the photogenerated electrons and holes. As a result, the more $^{\bullet}$OH and $^{\bullet}O_2^-$ radicals produced, the higher photocatalytic performance of the new photocatalyst $SrSn(OH)_6$ towards benzene was obtained. In addition, it has been reported that moisture, which mainly comes from the degradation products of benzene, may also play an important role in the catalytic cycle [14] (Eq. (B4)). $^{\bullet}$OH is commonly formed through the reaction of h^+ with surface —OH or absorbed H_2O. The hydroxyl structure of $SrSn(OH)_6$ can provide large quantities of —OH group and favors the capture and the adsorption of H_2O, which eventually benefits the form of $^{\bullet}$OH. Therefore, during the photocatalytic degradation of benzene, the production and consumption of electrons and holes were possibly following these reactions:

$$\text{Photocatalyst} + h\nu \rightarrow h^+ + e^- \quad \text{(B.1)}$$

$$h^+ + OH \rightarrow {}^{\bullet}OH \quad \text{(B.2)}$$

$$e^- + O_2 \rightarrow {}^{\bullet}O_2^- \quad \text{(B.3)}$$

$$h^+ + H_2O \rightarrow OH + H^+ \quad \text{(B.4)}$$

In addition to hydroxyl radical ($^{\bullet}$OH) and superoxide radical ($^{\bullet}O_2^-$), holes (h^+), electron (e^-) and dissolve oxygen also have influence to the photocatalytic degradation process. To investigate the role of above active species on the phtotcatalytic activity, the degradation of RhB over $SrSn(OH)_6$ (pH 9.2) with various scavengers were explored. After adding different scavengers, the photocatalytic reaction will be inhibited, which helps us to discriminate the importance of different active species in the photocatalytic process. Fig. 12 shows the photocatalytic activity of $SrSn(OH)_6$ (pH 9.2) towards the RhB degradation under the different conditions. *Tert*-butyl alcohol (TBA), used for quenching $^{\bullet}$OH, had the biggest inhibition to the degradation of RhB [20]. When 200 μL of TBA was added, the PCR was decreased to 16%. It proved that $^{\bullet}$OH played the most important role in the reaction system. When 1 mg of Benzoquinone (BQ) as a superoxide radical ($^{\bullet}O_2^-$) capturer was added in the system, the PCR was decreased to 54% [21]. It showed that the atmosphere of reaction was very important because the mount of dissolve oxygen would affect the production of $^{\bullet}O_2^-$. In order

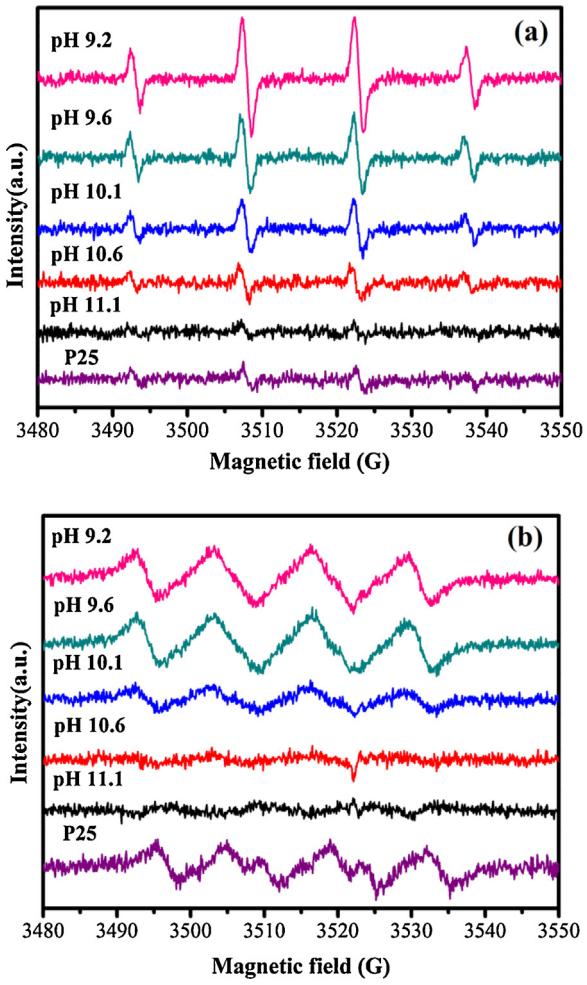

Fig. 11. ESR signals of the (a) DMPO-•OH and (b) DMPO-$•O_2^-$ in different pH values of $SrSn(OH)_6$ and P25 with irradiation, respectively.

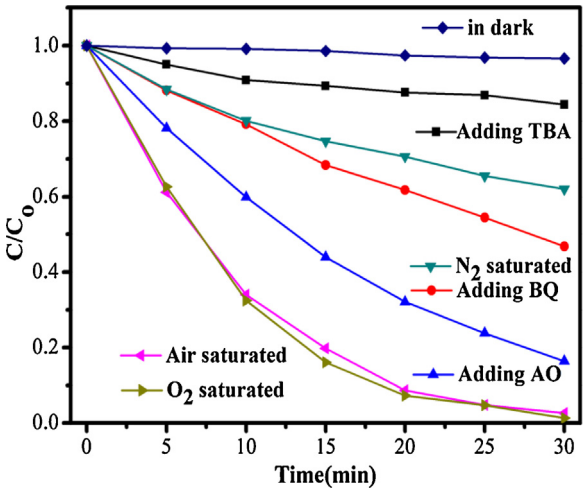

Fig. 12. Photocatalytic degradation of RhB over $SrSn(OH)_6$ in the different conditions exposed to UV light: adding 200 μL of TBA, 1 mg BQ, N_2 saturated, 0.1 g AO, air saturated and O_2 saturated (reaction temperature: 20 °C).

to better understand the effect of dissolve oxygen, the photocatalytic degradation under different gas condition had been done. The PCR of RhB in N_2-saturated and O_2-saturated were 38% and 99%, which meant that $•O_2^-$ play an important role in the photocatalytic degradation. It showed that the influence of dissolve oxygen to the reaction was smaller than to •OH the reaction. After 0.1 g of Ammonium oxalate (AO) as a hole-capturer was added in the system, it partially impacted the decomposition rate [22]. The PCR was decreased to 84%, which illuminated that holes make a little contribution to the degradation. Based on the above analysis, it can be concluded that the degradation of RhB was driven mainly by the participation of •OH and $•O_2^-$, holes to a lesser extent. Through the above analysis, the hydroxyl radical is the most important species, in accordance with the law of gas-phase reaction.

4. Conclusions

A new photocatalyst $SrSn(OH)_6$ have been synthesized at different pH value by a facile homogenous precipitation method for the first time. It presented a better photocatalytic performance toward benzene compared with commercial TiO_2 (P25). The reason why pH 9.2 showed a better performance than the other $SrSn(OH)_6$ samples can be explained in the three facets: first, the wider band gap provide a stronger oxidation potential, which enhances the redox ability of electrons and holes. Second, the larger surface area offers more activity sites to react with absorbed benzene. Third, the higher separation and transporting rate of photogenerated electrons and holes means more effective to produce more active radicals during the same time. Furthermore, through the test of ESR and the degradation of RhB with scavengers, the hydroxyl radical is confirmed to be the most important active radical in both degradation of benzene and RhB. Due to its high photocatalytic activity of organic pollutant and its simple synthesis method, the $SrSn(OH)_6$ and other hydroxide stannates would be further study in the environmental application by making good use of the hydroxyl groups in its structure.

Acknowledgment

This work was financially supported by the NNSF of China (21173047 and 21373049).

Appendix A. Supplementary data

Supplementary data associated with this article can be found, in the online version, at http://dx.doi.org/10.1016/j.apcatb.2015.09.051.

References

[1] J.D. Coates, R. Chakraborty, J.G. Lack, S.M. O'Connor, K.A. Cole, K.S. Bender, L.A. Achenbach, Nature 411 (2001) 1039–1043.
[2] H. Huang, D. Li, Q. Lin, W. Zhang, Y. Shao, Y. Chen, M. Sun, X. Fu, Environ. Sci. Technol. 43 (2009) 4164–4168.
[3] Q. Lan, L. Zhang, G. Li, R. Vermeulen, R.S. Weinberg, M. Dosemeci, S.M. Rappaport, M. Shen, B.P. Alter, Y. Wu, Science 306 (2004) 1774–1776.
[4] A. Fujishima, T.N. Rao, D.A. Tryk, J. Photochem. Photobiol. C Photochem. Rev. 1 (2000) 1–21.
[5] M.R. Hoffmann, S.T. Martin, W. Choi, D.W. Bahnemann, Chem. Rev. 95 (1995) 69–96.
[6] L. Ge, M. Xu, M. Sun, H. Fang, Mater. Res. Bull. 41 (2006) 1596–1603.
[7] J.-G. Yu, H.-G. Yu, B. Cheng, X.-J. Zhao, J.C. Yu, W.-K. Ho, J. Phys. Chem. B 107 (2003) 13871–13879.
[8] G. Martra, S. Coluccia, L. Marchese, V. Augugliaro, V. Loddo, L. Palmisano, M. Schiavello, Catal. Today 53 (1999) 695–702.
[9] R. Mendez-Roman, N. Cardona-Martínez, Catal. Today 40 (1998) 353–365.
[10] T. Yan, J. Long, X. Shi, D. Wang, Z. Li, X. Wang, Environ. Sci. Technol. 44 (2010) 1380–1385.
[11] Z. Li, Z. Xie, Y. Zhang, L. Wu, X. Wang, X. Fu, J. Phys. Chem. C 111 (2007) 18348–18352.
[12] S. Meng, D. Li, M. Sun, W. Li, J. Wang, J. Chen, X. Fu, G. Xiao, Catal. Commun. 12 (2011) 972–975.
[13] X. Fu, X. Wang, Z. Ding, D.Y. Leung, Z. Zhang, J. Long, W. Zhang, Z. Li, X. Fu, Appl. Catal. B: Environ. 91 (2009) 67–72.
[14] Y. Chen, D. Li, J. Chen, J. Wang, S. Meng, J. Xian, X. Fu, Y. Shao, Appl. Catal. B: Environ. 129 (2013) 403–408.

[15] H. Xue, Z. Li, L. Wu, Z. Ding, X. Wang, X. Fu, J. Phys. Chem. C 112 (2008) 5850–5855.
[16] X. Hu, Y. Tang, T. Xiao, J. Jiang, Z. Jia, D. Li, B. Li, L. Luo, J. Phys. Chem. C 114 (2009) 947–952.
[17] M. Butler, J. Appl. Phys. 48 (1977) 1914–1920.
[18] Y. Shaogui, Q. Xie, L. Xinyong, L. Yazi, C. Shuo, C. Guohua, Phys. Chem. Chem. Phys. 6 (2004) 659–664.
[19] A. Ye, W. Fan, Q. Zhang, W. Deng, Y. Wang, Catal. Sci. Technol. 2 (2012) 969–978.
[20] J. Wang, P. Wang, Y. Cao, J. Chen, W. Li, Y. Shao, Y. Zheng, D. Li, Appl. Catal. B: Environ. 136 (2013) 94–102.
[21] R. Palominos, J. Freer, M. Mondaca, H. Mansilla, J. Photochem. Photobiol. A: Chem. 193 (2008) 139–145.
[22] W. Li, D. Li, W. Zhang, Y. Hu, Y. He, X. Fu, J. Phys. Chem. C 114 (2010) 2154–2159.